Decay of gravity-capillary waves in air/water sheared turbulence

Francesco Zonta [a,b], Miguel Onorato [c], Alfredo Soldati [a,b,*]

[a] *Dept. of Elec., Manag. & Mechanical Engineering, University of Udine, Via delle Scienze 208, 33100 Udine, Italy*
[b] *Institute of Fluid Mechanics and Heat Transfer, TU Wien, 1060 Wien, Austria*
[c] *Dept. of Physics, University of Torino, Via Pietro Giuria 1, 10125 Torino, Italy*

ARTICLE INFO

ABSTRACT

Direct Numerical Simulation (DNS) is used to analyze the wave-decay process in a countercurrent air/water turbulent flow. Three dimensionless numbers describe the problem: the Reynolds number Re_τ (which measures the importance of inertia compared to viscosity), the Weber number We (which measures the importance of inertia compared to surface tension) and the Froude number Fr (which measures the importance of inertia compared to gravity). We keep Re_τ constant and we vary We and Fr. Regardless of the values of the physical parameters, we observe an initial exponential decay followed by the achievement of a new statistically stationary condition. The parameters characterizing this exponential decay do depend on the specific values of Re, Fr and We. Wavenumber spectra computed at different time instants during the wave decay process reveal that the spectral properties of waves change in time: starting from a condition characterized by the predominance of low-wavenumber waves, we observe a "blue shift" of the energy spectra towards higher wavenumbers, indicating the emergence of a strong capillary behavior. At the new asymptotic steady state condition, wave energy spectra are in fair agreement with the predictions given by the Wave Turbulence Theory. We also characterize the statistical behavior of the interface deformation to highlight the interplay between gravity and surface tension in determining the interface structure.

© 2016 Elsevier Inc. All rights reserved.

1. Introduction

Understanding the physics of the deformable interface separating air and water in two phase turbulent flows is of great importance in many industrial and environmental flows, from the design of condensers/evaporators to the prediction of air-sea interaction for climate studies. Most of the previous theoretical (Zakharov et al., 1992), experimental (Falcon et al., 2007a) and numerical (Dyachenko et al., 2004) studies of wave dynamics in two-phase air/water flows considered statistically-stationary state conditions. Much less is known about nonstationary wave turbulence, which however occurs in any transient situation from a stationary state to another due to a change in the external forcing condition of waves. This is the case of wave decay, developing when the external forcing applied to maintain the wave dynamics is suddenly reduced or removed (sudden change of wind conditions).

Despite its importance, experimental studies on the wave decay process of surface waves are only a few. Deike et al. (2012) analyzed the free decay of capillary waves on a fluid surface and found that the average amplitude of the free surface deformation decays exponentially in time as the wave maker is stopped. During the decay process, the authors observed that the wave spectrum maintains a self-similar slope consistent with that characterizing the steady state regime. These findings support the idea that each instantaneous realization of freely decaying capillary turbulence is similar to the steady state capillary turbulence, though with a decreasing energy content in time. Recently, Bedard et al. (2013) studied the raising and decaying process of surface gravity waves in a large laboratory flume. Relevant to the present study is the observation that the entire decay process is made of a short initial power-law decay followed by an exponential decay (due to viscous friction). The above-mentioned experimental studies confirm previous theoretical predictions made in the framework of Wave Turbulence Theory (WTT) on the decay rate of gravity and capillary waves and on the self similarity of the wave spectrum (Falkovich et al., 1995; Kolmakov, 2006; Zakharov et al., 1992). However, experimental results (with only few exception, see Berhanu and Falcon, 2013) are usually limited to local measurements of the interface displacements. Obtaining a time-resolved description of the entire interface deformation in space (distribution of the interface displacement and of the interface curvature) is still an open issue.

* Corresponding author.
  E-mail address: alfredo.soldati@tuwien.ac.at (A. Soldati).

In this context, Direct Numerical Simulation (DNS) can help providing the time evolution of the interface deformation together with a detailed description of the flow above and below the interface. This is extremely important for non-stationary wave conditions, where it is essential to record the coupled fluid/interface interaction in time and space. Unfortunately, direct numerical simulations of the wave decay process have never been performed in a coupled air/water flow systems.

To fill this gap, we propose here a DNS-based study on the wave decay process. We consider a countercurrent flow configuration, where air and water are driven by an imposed pressure gradient and flow in opposite directions. We employ the numerical technique already used in Zonta et al. (2015) to study the wave generation process. We start from an initial wavy interface and we let the system evolve by reducing the interfacial shear. After a transient exponential decay, a new asymptotic steady state condition is observed. We try to characterize the statistical properties of waves both during the transient decay and at the new asymptotic condition. We finally highlight the role of gravity and surface tension in determining the interface deformation.

## 2. Governing equations and numerical modeling

With reference to the schematics of Fig. 1, we consider a turbulent air-water two-phase flow. The air and water phases are separated by a deformable interface and flow in opposite directions under the influence of an imposed pressure gradient. We use a cartesian coordinate system, with the streamwise, spanwise and interface-normal directions being denoted by $x-$, $y-$ and $z-$ respectively. Assuming newtonian and incompressible fluids, the dimensionless continuity and Navier–Stokes equations are:

$$\nabla \cdot \mathbf{u} = 0, \tag{1}$$

$$\frac{\partial \mathbf{u}}{\partial t} + \mathbf{u} \cdot \nabla \mathbf{u} = -\nabla p + \frac{1}{Re_\tau}\nabla^2\mathbf{u}, \tag{2}$$

where $\mathbf{u}$ is velocity, p is pressure and Re_τ is the shear Reynolds number (properly defined later). The reference quantities employed to obtain dimensionless variables in each subdomain (air and water) are the shear velocity $u_\tau = \sqrt{\tau_{int}/\rho}$ (τ_{int} being the shear stress at the interface and ρ the fluid density), the kinematic viscosity ν and the half depth of each subdomain h.

The numerical methodologies available to capture the interface dynamics belong to two different categories. The interface can be described using an approximate approach (where the interface is considered a thin transition layer) or using an exact sharp approach (where the interface is a zero-thickness layer). Examples
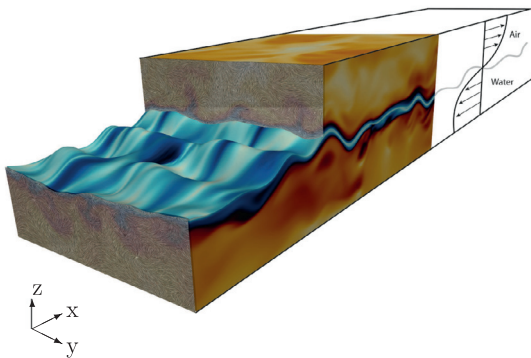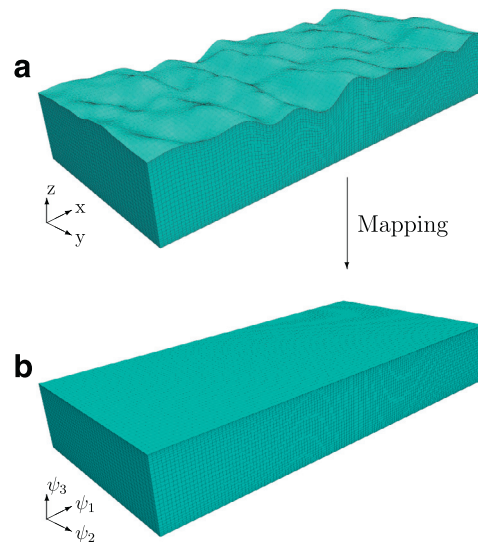
of approximate numerical approaches include Level Set (LS), Phase Field (PF), Volume of Fluid (VOF) and Front Tracking (FT) methods. We will briefly discuss only VOF, due to their widespread use in the description of surface waves. VOF methods are based on a concentration field C defined at the center of each computational cell. The concentration C assumes uniform values $C = 1$ and $C = 0$ in the bulk fluids, whereas $0 < C < 1$ in the cells crossed by the interface. Suitable reconstruction algorithms are required to obtain the correct shape of the interface from the value of C. The accuracy/efficiency of these algorithms is crucial to avoid a wrong estimate of the local normal vector n and of the local curvature (which are indeed important in the computation of capillary forces).

In the exact sharp approach, the fluid properties change sharply from one fluid to the other when crossing the zero-thickness interface. Differently from the approximate methods mentioned above, in this case boundary conditions must be prescribed at the moving interface. The only numerical method that can be used to obtain a sharp description of the interface is a fully resolved boundary fitted method (as the one employed in the present work). Boundary fitted methods are based on the advection of interfacial points subject to an external velocity (and stress) field. Once the position of the interfacial points is updated, the domain is deformed. A domain mapping technique must be used to transform the deformed domain into a cartesian one when a Fourier/Chebyshev pseudospectral solver is adopted to solve the governing equations of the flow (as in the present case). Note that this combined approach maintains a spectral accuracy with negligible numerical dissipation/dispersion. A detailed presentation of the numerical method is provided in the following.

In the present case, the distorted physical domain (x, y, z, t) is mapped into a rectangular parallelepiped in the computational domain (ψ_1, ψ_2, ψ_3, τ) using an algebraic mapping (De Angelis et al., 1997)

$$\psi_1 = x, \quad \psi_2 = y, \quad \psi_3 = \frac{z}{h + \eta(x, y, t)}, \quad \tau = t, \tag{3}$$

where η is the function describing the deformed interface boundary (see Fig. 2). Governing equations can be transformed from the physical space $X = (x, y, z, t)$ to the computational space

Fig. 1. Sketch of the physical domain: water (resp. air) flows below (resp. above) the interface. Water and air are driven by a fixed pressure gradient and flow in opposite directions. Note that the interface deformation has been magnified ($\times$ 100).

Fig. 2. Physical and computational domain: the deformed physical domain (x, y, z) is transformed into a cartesian computational domain (ψ_1, ψ_2, ψ_3) using a proper coordinate transformation (mapping).

$\Psi = (\psi_1, \psi_2, \psi_3, \tau)$ through the Jacobian of the transformation

$$J = \frac{\partial \Psi}{\partial X}. \tag{4}$$

Derivatives in the physical space can therefore be computed as $\partial_X = J \cdot \partial_\Psi$, with $\partial_X = (\partial/\partial x, \partial/\partial y, \partial/\partial z)^T$ and $\partial_\psi = (\partial/\partial \psi_1, \partial/\partial \psi_2, \partial/\partial \psi_3)^T$. A two-stage fractional-step method is used to discretize the governing balance equations in time. In the first step, a provisional velocity field $\tilde{\mathbf{u}}$ is obtained by solving the reduced momentum equation (without the pressure contribution)

$$\frac{\tilde{\mathbf{u}} - \mathbf{u}^n}{\Delta t} + \sum_{q=0}^{M-1} \alpha_q \nabla \cdot (\mathbf{u}\mathbf{u})^{n-q} - \frac{1}{2Re_\tau} \nabla^2 (\tilde{\mathbf{u}} + \mathbf{u}^n) = 0, \tag{5}$$

where the superscripts n and $n-1$ indicate two previous time levels. The convective term is treated explicitly using an Adams–Bashfort scheme ($M = 2$, $\alpha_0 = 3/2$, $\alpha_1 = -1/2$), whereas an implicit Crank–Nicolson scheme is used for the viscous term. The provisional velocity field $\tilde{\mathbf{u}}$ is then corrected using the equation

$$\frac{\mathbf{u}^{n+1} - \tilde{\mathbf{u}}}{\Delta t} + \nabla p^{n+1} = 0, \tag{6}$$

with the superscript $n+1$ indicating the variables at the new time step (unknown). Taking the divergence of Eq. (6) and imposing that the velocity field at the new time step ($\mathbf{u}^{n+1}$) must be divergence-free, we obtain

$$\nabla^2 p^{n+1} = \frac{1}{\Delta t} \nabla \cdot \tilde{\mathbf{u}}, \tag{7}$$

which can be solved to give p^{n+1} and, from Eq. (6), $\mathbf{u}^{n+1}$. For the spatial discretization of the governing balance equations, we employed a pseudospectral technique, based on transforming a generic field variable $\Phi(\psi_i)$ into wavenumber space using Fourier transform in the $\psi_{1,2}$ directions and Chebyshev transform in the ψ_3 direction:

$$\Phi(\psi_i) = \sum_{k_1, k_2, n_3} \hat{\Phi}(k_1, k_2, n_3) e^{i(k_1 \psi_1 + k_2 \psi_2)} T_{n3}(\psi_3), \tag{8}$$

where $\hat{\Phi}$ indicates the spectral amplitude of the variable, and $T_{n3} = \cos[n_3 \cos^{-1}(\psi_3/h)]$ are Chebyshev polynomials. The discretized governing equations for $\hat{\mathbf{u}}$ are:

$$\left(\frac{d^2}{d\xi_3^2} - \beta \right) \hat{u}_i = \frac{\hat{H}_i}{\delta} - F\left(\nabla_{off}^2 u_i^n \right), \tag{9}$$

where $\hat{H}_i$ is given by

$$\hat{H}_i = \Delta t \left(\frac{3}{2} \hat{S}_i^n - \frac{1}{2} \hat{S}_i^{n-1} \right) + F\left(\delta \nabla_{diag}^2 u_i^n \right) + \hat{u}_i^n, \tag{10}$$

S_i^n are the convective terms, whereas $\beta = \frac{1+\delta k^2}{\delta}$ and $\delta = \frac{\Delta t}{2Re_\tau}$ (Δt is the time-step). Terms $F(\cdot)$ represent the Fourier-Chebyshev transform of a function in the computational space Ψ. The terms ∇_{diag}^2 and ∇_{off}^2 arise from the mapping procedure and indicate, respectively, the diagonal and the off-diagonal terms of the Laplacian operator ∇^2. For the pressure field $\hat{p}^{n+1}$ we have:

$$\left(\frac{d^2}{d\xi_3^2} - \beta \right) \hat{p}^{n+1} = \frac{F\left(\nabla \cdot \hat{\mathbf{u}} \right)}{\Delta t} - F\left(\nabla_{off}^2 p^n \right). \tag{11}$$

The discretized equations (Eqs. (9)–(11)) are solved using a Chebyshev-Tau method after imposing appropriate boundary conditions (Soldati and Banerjee, 1998; Zonta et al., 2012). Periodicity is employed in the streamwise (ξ_1) and spanwise (ξ_2) directions. At the interface, both a kinematic and a dynamic boundary condition must be enforced (Zonta et al., 2015). A kinematic boundary condition for the interface prescribes that the interface is material,

$$\frac{\partial \eta}{\partial t} + u_x \frac{\partial \eta}{\partial x} + u_y \frac{\partial \eta}{\partial y} = u_z, \tag{12}$$

Table 1
Wave decay in a countercurrent air-water flow: summary of the simulations parameters.

	S1	S2	S3
h [m]	0.04	0.05	0.06
$u_{\tau L}$ [m/s]	1.29×10^{-3}	1.03×10^{-3}	0.86×10^{-3}
$u_{\tau G}$ [m/s]	3.86×10^{-2}	3.09×10^{-2}	2.58×10^{-2}
Re_τ	170	170	170
Fr	4.23×10^{-6}	2.17×10^{-6}	1.25×10^{-6}
We	9.52×10^{-4}	7.62×10^{-4}	6.35×10^{-4}
$\sqrt{Fr}/We$	2.16	1.93	1.4
Grid	$256 \times 128 \times 129$	$256 \times 128 \times 129$	$256 \times 128 \times 129$

with η representing the interface amplitude with respect to the mean fluid height h. This equation is integrated in time to track the interface motion and to compute the mapping coefficients. A dynamic boundary condition prescribes the continuity of the velocity vector and of the normal/shear components of the stress tensor (Fulgosi et al., 2003; Lombardi et al., 1996)

$$\begin{cases} \frac{1}{Re_\tau}((\tau_{\mathbf{L}} - \tau_{\mathbf{G}}) \cdot \mathbf{n}) \cdot \mathbf{n} + p_G - p_L + \frac{1}{We} \nabla \cdot \mathbf{n} - \frac{1}{Fr} \eta = 0 \\ ((\tau_L - \tau_G) \cdot \mathbf{n}) \cdot \mathbf{t}_i = 0, \ i = 1, 2 \\ \mathbf{u}_G = \frac{1}{\mathcal{R}} \mathbf{u}_L, \end{cases} \tag{13}$$

where the subscripts G and L are for gas and liquid respectively, τ is the viscous stress tensor, $\mathbf{n}$ and $\mathbf{t}_i$ are the normal and the two tangential unit vectors to the interface and $\mathcal{R} = \sqrt{\rho_L/\rho_G}$ is the density ratio. The Weber (We), Froude (Fr) and Reynolds (Re_τ) numbers are defined as:

$$We = \frac{\rho_L h u_{\tau L}^2}{\gamma}, \quad Fr = \frac{\rho_L u_{\tau L}^2}{gh(\rho_L - \rho_G)}, \quad Re_\tau = \frac{u_{\tau G} 2h}{\nu_G} = \frac{u_{\tau L} 2h}{\nu_L}, \tag{14}$$

where γ is the surface tension, g is the acceleration due to gravity and u_τ is evaluated at the beginning of the simulation. At the outer boundaries in the interface-normal direction (ψ_3), free-slip boundary conditions are applied.

2.1. Simulations

The coupled air/water flow is assumed at atmospheric pressure and at a mean temperature $\theta = 50°C$ (typical of industrial/chemical systems). The physical properties of the system (air and water) are evaluated at these reference conditions: the density ratio is $\mathcal{R} = 29.9$ and the surface tension is $\gamma = 0.0679$ N/m. The computational domain, whose size is $4\pi h \times 2\pi h \times 2h$, is discretized using $256 \times 128 \times 129$ nodes (for each phase) in the x, y and z direction, respectively. We run three different simulations, keeping Re_τ constant ($Re_\tau = 170$) and varying Fr and We: $Fr = 2.1 \times 10^{-6}$ and $We = 4.7 \times 10^{-4}$ for simulation $S1$; $Fr = 1.1 \times 10^{-6}$ and $We = 3.8 \times 10^{-4}$ for simulation $S2$; $Fr = 6.25 \times 10^{-7}$ and $We = 3.2 \times 10^{-4}$ for simulation $S3$. An overview of the simulation parameters is provided in Table 1.

3. Results

We consider the transient decay of waves due to a sudden change of the external wave forcing. To do this, we run a preliminary simulation to obtain a fully-developed wave field. This simulation is characterized by an interfacial shear velocity $u_{\tau G} = 4.42 \times 10^{-2}$ (quantifying the strength of the wind shear) and by waves having a root mean square (rms) of the interface displacement $\eta_0 = 2 \times 10^{-3}$. Starting from this initial condition, we reduce the shear at the interface (i.e. we change the flow parameters to
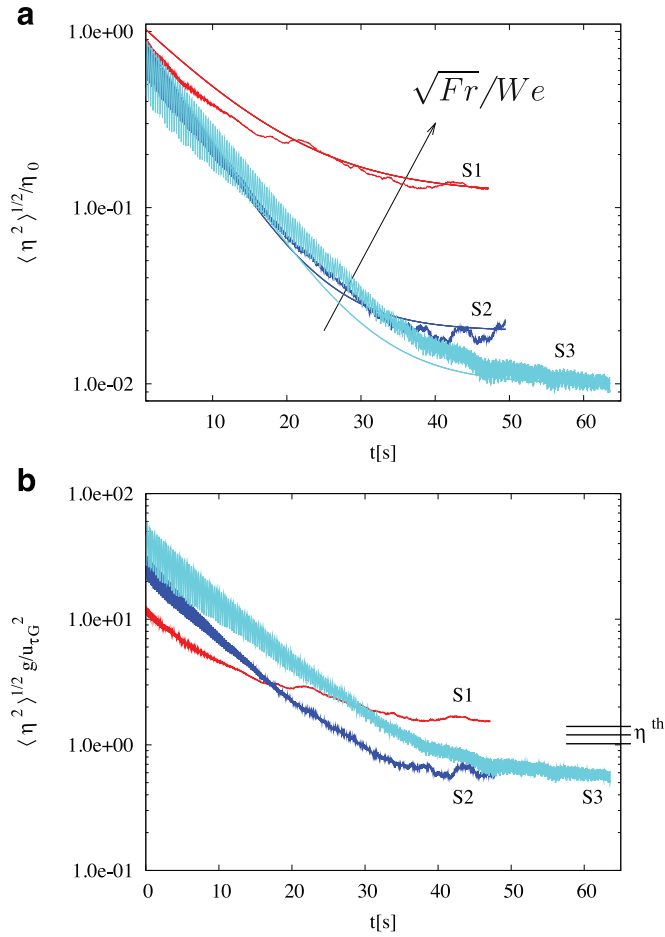
Fig. 3. Panel a: Time behavior of root mean square (rms) of the surface elevation, $\langle\eta(t)^2\rangle^{1/2}$, normalized by its initial amplitude η_0; the analytical results obtained with the exponential model of the wave decay ($\langle\eta(t)^2\rangle^{1/2} = \eta_0\exp(-t/\tau) + \eta_\infty$) are also shown (thin lines). Panel b: Time behavior of $\langle\eta(t)^2\rangle^{1/2}$ made dimensionless by $g/u_{\tau G}^2$. The theoretical values predicted by the simplified model (Eq. (18)) are labeled as η^{th}.

obtain a reduction of the wind shear at the interface). The wave decay process is quantified in Fig. 3a by computing the behavior of the rms of the interface elevation, $\langle\eta(t)^2\rangle^{1/2}$, normalized by the initial values η_0. Starting from η_0, $\langle\eta(t)^2\rangle^{1/2}$ decays rapidly ($t < 30$ s) before attaining a new statistically stationary condition. The wave decay process can be modeled as an exponential decay given by $\langle\eta(t)^2\rangle^{1/2} = \eta_0\exp(-t/\tau) + \eta_\infty$ (thin lines in Fig. 3a), where τ is a characteristic relaxation time of the wave decay process, whereas η_∞ is the asymptotic value of the wave amplitude. The two parameters η_∞ and τ of the exponential model do depend on the specific values of $\sqrt{Fr}/We$ (η_0 being the same for each simulation): $\tau = 10$ and $\eta_\infty = 0.12$ for $\sqrt{Fr}/We = 2.16$ (S1), $\tau = 4$ and $\eta_\infty = 0.02$ for $\sqrt{Fr}/We = 1.93$ (S2) while $\tau = 3$ and $\eta_\infty = 0.01$ for $\sqrt{Fr}/We = 1.4$ (S3). At the new steady state condition, waves with larger values of $\sqrt{Fr}/We$ are characterized by larger amplitudes. The wave amplitude $\langle\eta(t)^2\rangle^{1/2}$ can be conveniently rescaled (Alves et al., 2003; Janssen, 2004) as $\langle\eta(t)^2\rangle^{1/2}g/u_{\tau G}^2$ to identify possible scaling laws (see Fig. 3b). We try to estimate the asymptotic amplitude of waves considering an energetic balance at the air/water interface. The energy of the interface is stored into kinetic (E_k) and potential energy (E_p). Potential energy consists of two different contributions, one due to gravity, $E_{p,g}$, and one due to surface tension, $E_{p,\gamma}$ (Guo and Shen, 2010; Kundu et al., 2012):

$$E_k = \frac{1}{2}S\rho_L g\langle\eta^2\rangle \tag{15}$$

$$E_{p.g} = \frac{1}{S}\int_S \rho_L g\eta^2 dS - \frac{1}{S}\int_S \rho_G g\eta^2 dS \simeq \frac{1}{2}S\rho_L g\langle\eta^2\rangle \tag{16}$$

$$E_{p.\gamma} = \frac{\gamma}{S}\int_S\left[\sqrt{1 + \left(\frac{\partial\eta}{\partial x}\right)^2 + \left(\frac{\partial\eta}{\partial y}\right)^2} - 1\right]dS \simeq \frac{1}{2}\gamma Sk_c^2\langle\eta^2\rangle \tag{17}$$

where the wave number associated to capillary effects is $k_c = \frac{2\pi}{\lambda_c} \simeq 370\,\mathrm{m}^{-1}$ and is linked to the inverse of the capillary wave length $\lambda_c = \sqrt{\frac{4\pi^2\gamma}{g\rho}} \simeq 1.7\times10^{-2}$ m on a water interface. The total energy of the interface $E_t = E_k + E_g + E_\gamma = S\rho_L g\langle\eta^2\rangle + \frac{1}{2}S\gamma k_c^2/2\langle\eta^2\rangle$ is provided by the shear stress acting on it $E_{shear} = \tau_s S = \rho_G u_{\tau G}^2 S$. From the energy balance, $E_{shear} = E_t$, we obtain:

$$\langle\eta^2\rangle_{th}^{1/2} = \left[\frac{\rho_G u_{\tau G}^2 2\pi h}{\left(\rho_L g + \frac{\gamma k_c^2}{2}\right)}\right]^{1/2}. \tag{18}$$

The dimensionless values $\langle\eta^2\rangle_{th}^{1/2}(g/u_{\tau G}^2)$ are reported in Fig. 3b together with the computational results.
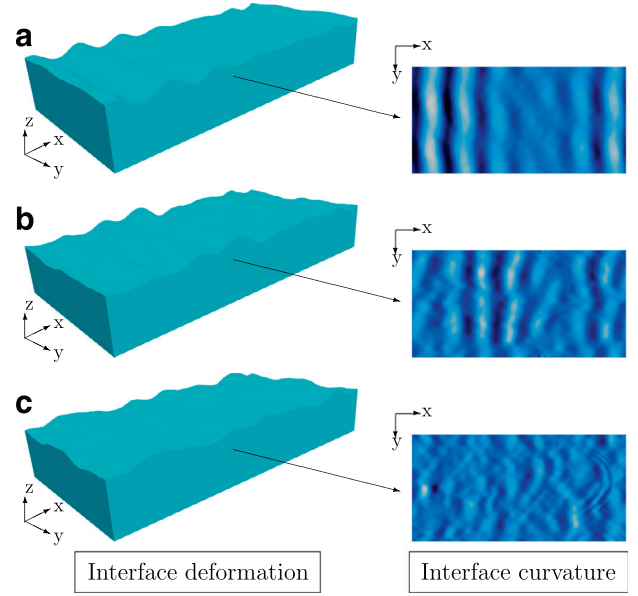
The theoretical predictions are in fair agreement with the numerical results, indicating that Eq. (18) can be used to estimate $\langle\eta^2\rangle^{1/2}$ in sheared air/water flows. Larger deviations from the theoretical values are observed for S2 and S3, likely due to a more complex interface morphology and interface/turbulence interaction (viscous dissipation) which prevents from assuming the simplified expressions provided in Eq. (15)–(17).

To deepen the analysis of the transient decay of interfacial waves, we compute the time behavior of the root mean square (rms) of the interface curvatures along the streamwise $\langle\eta_{xx}(t)^2\rangle^{1/2}$ and spanwise $\langle\eta_{yy}(t)^2\rangle^{1/2}$ directions. The time behavior of $\langle\eta_{xx}(t)^2\rangle^{1/2}$ (Fig. 4a) is similar to that of $\langle\eta(t)^2\rangle^{1/2}$ (exponential decay) and is characterized by an asymptotic value that increases for increasing $\sqrt{Fr}/We$. By contrast, the time behavior of $\langle\eta_{yy}(t)^2\rangle^{1/2}$ has a much shorter transient decay (Fig. 4b) when compared to that of $\langle\eta_{xx}(t)^2\rangle^{1/2}$. The difference between the magnitude of $\langle\eta_{xx}(t)^2\rangle^{1/2}$ for $\sqrt{Fr}/We = 2.16$ (S1) and $\sqrt{Fr}/We = 1.4$ (S3) is remarkably reduced for $\langle\eta_{yy}(t)^2\rangle^{1/2}$. The prominence of $\langle\eta_{xx}(t)^2\rangle^{1/2}$ compared to $\langle\eta_{yy}(t)^2\rangle^{1/2}$ seems to indicate that waves propagate essentially along the streamwise direction for $\sqrt{Fr}/We = 2.16$ (S1). As $\sqrt{Fr}/We$ is decreased, waves propagate also in the spanwise direction and $\langle\eta_{yy}(t)^2\rangle^{1/2}$ becomes comparable to $\langle\eta_{xx}(t)^2\rangle^{1/2}$. To quantify the increased importance of $\langle\eta_{yy}(t)^2\rangle^{1/2}$ compared to $\langle\eta_{xx}(t)^2\rangle^{1/2}$ and to estimate the complexity of the interface morphology, we compute the ratio between the streamwise and the spanwise curvature, $\langle\eta_{yy}(t)^2\rangle^{1/2}/\langle\eta_{xx}(t)^2\rangle^{1/2}$ (Fig. 4c). For $\sqrt{Fr}/We = 2.16$ (S1), $\langle\eta_{yy}(t)^2\rangle^{1/2}/\langle\eta_{xx}(t)^2\rangle^{1/2} \simeq 0.2$, and the interface behaves as a monodimensional wave traveling along the streamwise direction ($\langle\eta_{xx}(t)^2\rangle^{1/2}$ larger compared to $\langle\eta_{yy}(t)^2\rangle^{1/2}$). For decreasing $\sqrt{Fr}/We$ (simulations S2 and S3), the surface tension becomes more important and the interface behaves as a two-dimensional rough interface characterized by waves traveling along the x and y directions ($\langle\eta_{yy}(t)^2\rangle^{1/2}$ and $\langle\eta_{xx}(t)^2\rangle^{1/2}$ have the same order of magnitude). This situation is clearly visualized in Fig. 5, where we show the interface deformation and the corresponding interface curvature for each simulation: the interface deformation is larger along the streamwise direction for $\sqrt{Fr}/We = 2.16$, whereas it is more isotropic (interface roughness) for decreasing $\sqrt{Fr}/We$. We quantify explicitly this behavior by looking at the two dimensional wavenumber spectrum $E(k_x, k_y, t)$ for simulations $S1$ (Fig. 6a) and $S3$ (Fig. 6b). Results are computed considering the last snapshot of each simulation. It is clear that for simulation $S1$ wave energy is concentrated in few small wavenumber components in the range $60 < k_x < 100\,m^{-1}$ and for $k_y = 0$. This

a

b

c
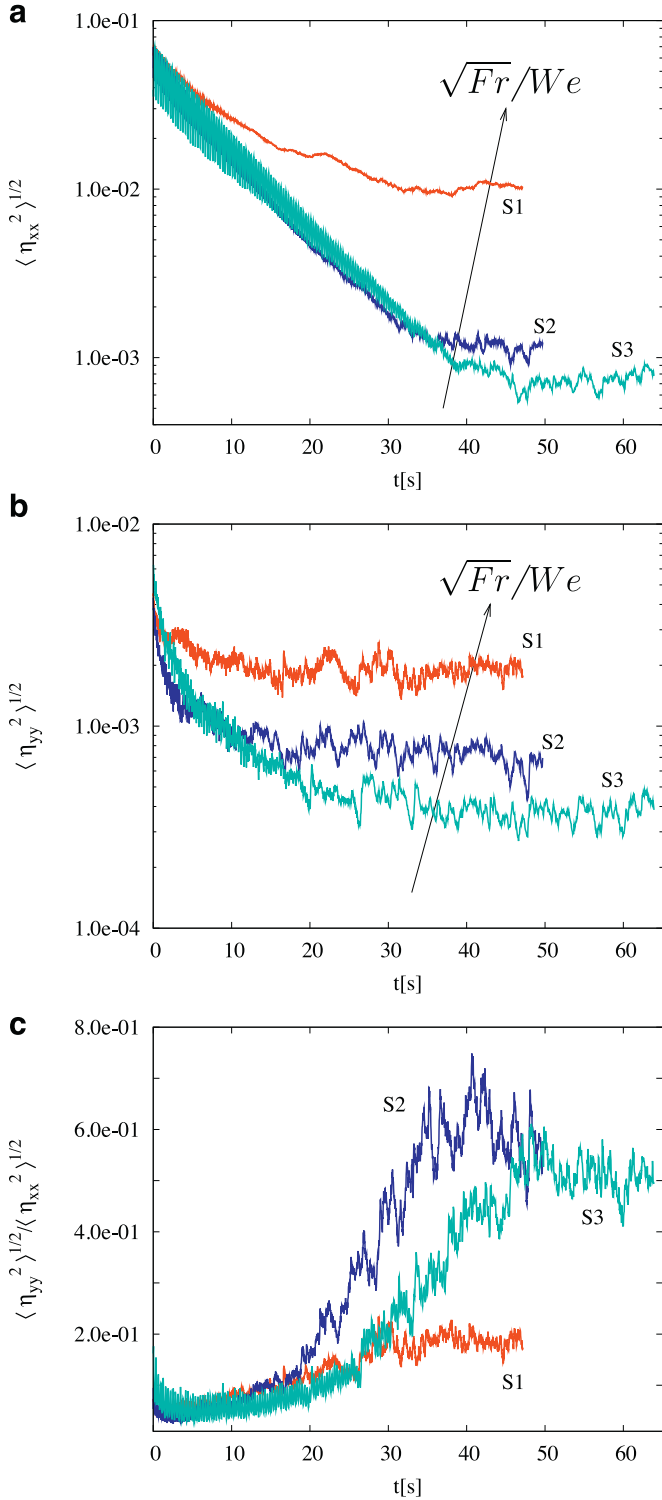
Fig. 4. Time behavior of the rms of the interface curvature along the streamwise direction, $\langle\eta_{xx}(t)^2\rangle^{1/2}$ (panel a) and along the spanwise direction, $\langle\eta_{yy}(t)^2\rangle^{1/2}$. Panel c: Time behavior of the ratio $\langle\eta_{yy}(t)^2\rangle^{1/2}/\langle\eta_{xx}(t)^2\rangle^{1/2}$.

a

Interface deformation   Interface curvature

Fig. 5. Interface deformation (η, left) and interface curvature along the streamwise direction (η_{xx}, right) for each simulation. Panels: (a) simulation S1; (b) simulation S2; (c) simulation S3. The amplitude of the interface deformation has been magnified $\times$ 3 for simulation S1, $\times$ 30 for simulation S2 and $\times$ 60 for simulation S3.

a

b
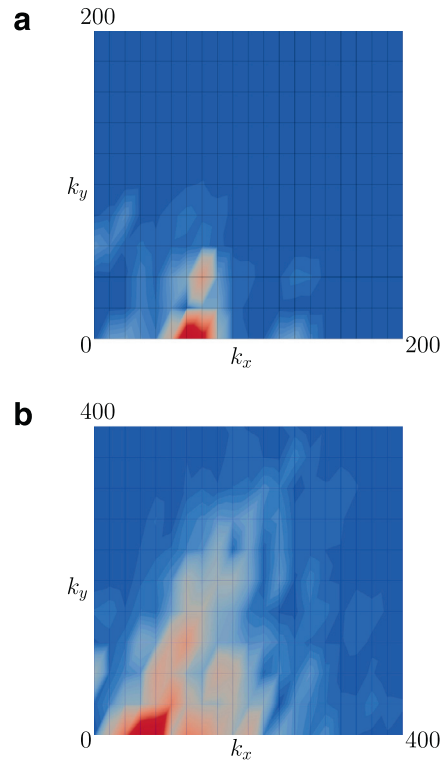
Fig. 6. Two dimensional wavenumber spectrum $E(k_x, k_y, t)$ computed at the final snapshot of simulations S1 (panel a) and S3 (panel b).

indicates that waves move preferentially along the streamwise direction ($k_x \neq 0$, $k_y = 0$). The situation is different for simulation S3, with wave energy being almost evenly distributed over a broad range of wavenumbers along both k_x and k_y. In particular we observe a more isotropic spectrum, with the activation of waves traveling also along the spanwise direction ($k_y \neq 0$).
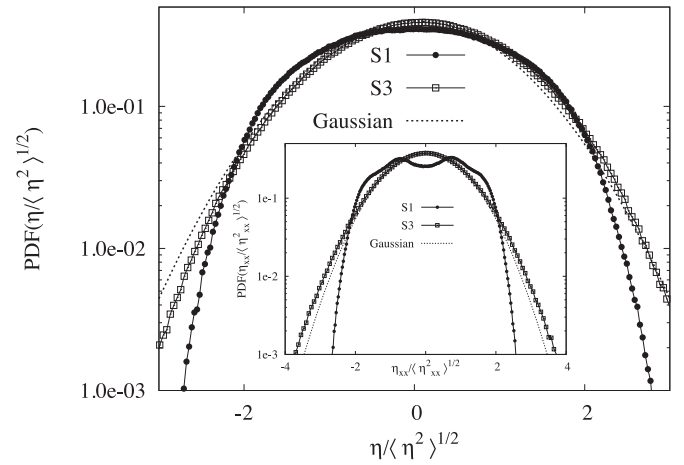
During the wave decay process, the spectral properties of the interface vary in time. We quantify these variations by computing the behavior of the wavenumber spectrum $E(k_x, t) = \int_{k_y} E(k_x, k_y, t) \mathrm{d}k_y$ at the beginning and at the end of the simulation for $\sqrt{Fr}/We = 2.16$ (S1) and for $\sqrt{Fr}/We = 1.4$ (S3). Results are shown as a function of the wavenumber in the streamwise direction k_x in the insets of Fig. 7. For $\sqrt{Fr}/We = 2.16$ (inset of Fig. 7a), we essentially observe an attenuation of the wave
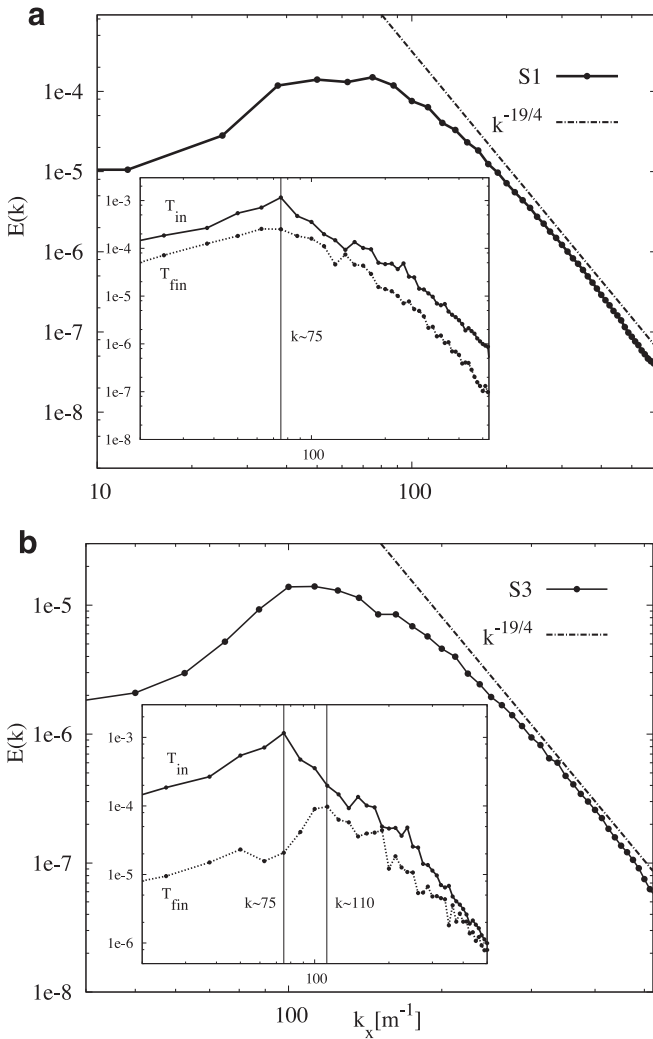
Fig. 7. Wavenumber spectrum for simulations $S1$ (panel a), and $S3$ (panel b). The main panels show the wavenumber spectrum, $E(k_x)$ = $1/(\Delta T) \int_t \int_{k_y} \eta(k_x, k_y, t) dk_y dt$, averaged in time over a period $\Delta T = 15\,s$ after the wave decay process is completed. Insets show the behavior of the instantaneous wavenumber spectrum $E(k_x, t) = \int_{k_y} \eta(k_x, k_y, t) dk_y$ computed at the beginning (solid line) and at the end (dotted line) of the simulation.

Fig. 8. Probability density function (PDF) of the normalized interface elevation $\eta/\langle \eta^2 \rangle^{1/2}$ for simulations S1 and S3. Inset: PDF of the normalized interface curvature $\eta_{xx}/\langle \eta_{xx}^2 \rangle^{1/2}$. Gaussian curve with zero mean and unit standard deviation (dotted line).

amplitude, with the maximum of the spectrum occurring always at $k \simeq 75\,m^{-1}$. The situation changes for $\sqrt{Fr}/We = 1.4$ (Fig. 7b). In this case, the maximum moves from $k \simeq 75\,m^{-1}$ toward $k \simeq 110\,m^{-1}$, hence indicating that the wave energy is not only reduced (due to the wave decay) but it is also partially transferred toward small capillary waves. After the entire process of wave decay, the interface attains a new statistically stationary regime. We characterize the structure of the interface in this new regime by computing the time-averaged wavenumber spectrum $E(k_x) = 1/(\Delta T) \int_t \int_{k_y} E(k_x, k_y, t) dk_y dt$ (with $\Delta T = 15\,s$). Results are shown in the main panels of Fig. 7 for simulation S1 (Fig. 7a) and for simulation S3 (Fig. 7b). We clearly observe the presence of a $k_x^{-19/4}$ power law, which is consistent with the theoretical predictions given by WTT in the capillary regime (Pushkarev and Zakharov, 1996; Zonta et al., 2015). Our spectra in the capillary range scale as $k_x^{-19/4}$ instead of $k^{-15/4}$ due to the directional averaging over k_y. Recovering of a power-law energy spectrum close to the predictions of WTT has been also observed during the wave-decay process in an elastic plate (Miquel and Mordant, 2011).

The establishment of the energy cascade during and after the exponential decay can be explained as follows: (i) The most ener-getic waves decay exponentially in time, due to viscous dissipation; (ii) the energy to sustain capillary waves is small compared to the energy contained in the most energetic waves. Therefore, although a large proportion of energy is damped by viscous dissipation and decays exponentially in time, there is still enough energy to feed the (power law) cascade towards the smallest scales. The observation that for decreasing $\sqrt{Fr}/We$ capillarity increases importance compared to gravity can also be assessed by looking at the Bond number $Bo = \rho_L g/(\gamma k^2)$ (Deike et al., 2015), with the characteristic wavenumber taken here as the wavenumber at which the energy spectrum develops a peak. Note that the Bond number measures the relative importance of forces induced by gravity and surface tension. The smaller is Bo, the larger are capillary effects. In the present case, Bo ranges between $Bo = 90$ (simulation $S1$) to $Bo = 14$ (simulation $S3$). This suggests that capillary effects become increasingly important for decreasing $\sqrt{Fr}/We$.

To characterize further the topological properties of the interface at the steady-state condition, we compute the probability density function (PDF) of the interface amplitude normalized by the corresponding standard deviation, $\langle \eta^2 \rangle^{1/2}$. Results are shown in the main panel of Fig. 8 for simulation with $\sqrt{Fr}/We = 2.16$ (S1) and with $\sqrt{Fr}/We = 1.4$ (S3). Together with the DNS data we show the PDF of a gaussian distribution with zero mean, unit standard deviation and unit integral. Note that the integral of a gaussian distribution is $I_G = \int_{-\infty}^{\infty} \exp(-x^2/2) dx = 2 \cdot \sqrt{\pi/2}$. Although being characterized by a completely different shape, distributions from both the simulations are roughly symmetric. For $\sqrt{Fr}/We = 1.4$ (S3), we note that the PDF is close to a gaussian distribution, which suggests that nonlinear effects are not sufficiently strong to break the symmetrical distribution of wave amplitudes (Falcon et al., 2007b). Interestingly, for $\sqrt{Fr}/We = 2.16$ (S1) the PDF departs from gaussianity, indicating that the interface deformation is far from a random distribution. As previously discussed, it is closer to a monochromatic wave traveling along the streamwise direction producing a subgaussian distribution. To quantify the degree of subgaussianity, we use the excess kurtosis $e = \eta^4/((\langle \eta^2 \rangle^{1/2})4 - 3$ ($e = 0$ for a Gaussian distribution). In the present case, we found $e = -1.6$ for S1 and $e = -0.8$ for S3.

The distribution of the interface deformation influence the distribution of the interface curvature. In the inset of Fig. 8 we show the PDF of the streamwise curvature $\eta_{xx}/\langle \eta_{xx}(t)^2 \rangle^{1/2}$ for $\sqrt{Fr}/We = 2.16$ (S1) and for $\sqrt{Fr}/We = 1.4$ (S3). As expected, the normalized $PDF(\eta_{xx})$ is almost gaussian for $\sqrt{Fr}/We = 1.4$ (S3), with the
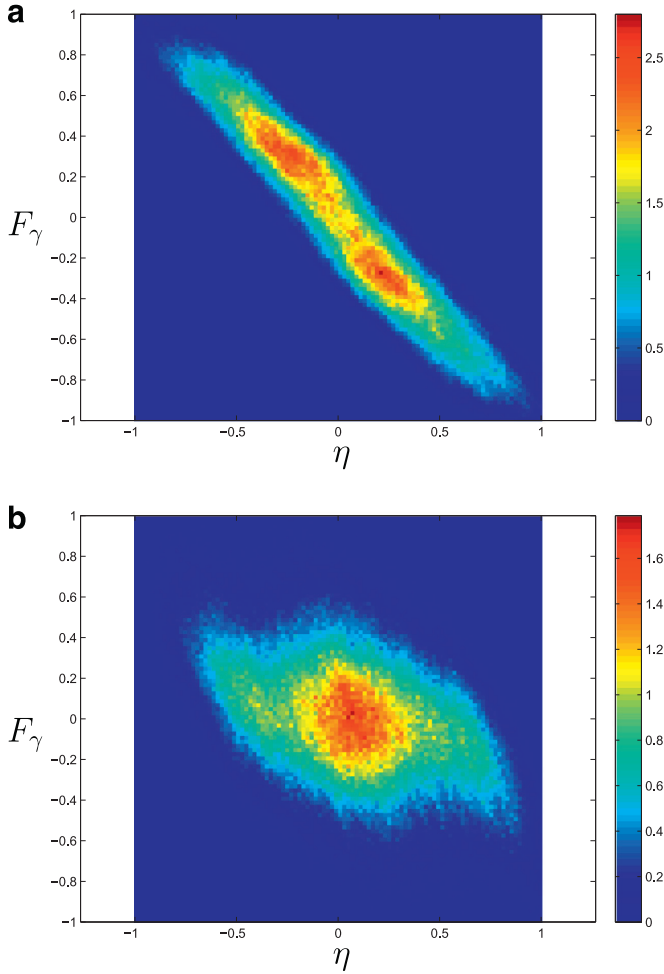
Fig. 9. Joint PDF between the interface elevation η and the capillarity $F_\gamma = We^{-1}\nabla \cdot n$. Panels: (a) simulation S1; (b) simulation S3.

Fig. 10. Coherency spectrum between the interface elevation η and the capillarity (F_γ). Each panel corresponds to a different simulation: (a) simulation S1; (b) simulation S2; (c) simulation S3.

most probable value $\eta_{xx}/\langle\eta_{xx}(t)^2\rangle^{1/2} = 0$. This reflects the fact that, when the surface tension dominates, the interface behaves as a surface roughness characterized by a gaussian distribution of curvatures. The situation is largely different for $\sqrt{Fr}/We = 2.16$ (S1). In this case, we observe two sharp peaks, one positive and one negative ($\eta_{xx}/\langle\eta_{xx}(t)^2\rangle^{1/2} \simeq \pm 1$), corresponding to crests and throats of a traveling monochromatic wave. Regions of lower and higher curvatures are instead characterized by a remarkably lower frequency of occurrence.

The distribution of the interface curvature is directly linked to the distribution of the capillarity force $F_\gamma = We^{-1}\nabla \cdot n$ acting as a restoring force of interfacial waves. As a consequence, a connection can be established between the interface elevation η and the capillarity force F_γ. To analyze this connection, we measure the joint probability distribution function (JPDF) between η and F_γ. The contour maps of the JPDF, shown in Fig. 9, clearly indicate that the $\eta - F_\gamma$ coupling mechanism depends on the values of the physical parameter $\sqrt{Fr}/We$. For larger $\sqrt{Fr}/We$ (simulation S1, Fig. 9a) the contour maps of the JPDF are inclined by $-\pi/4$, indicating that there is a strong negative correlation between the interface elevation and the capillarity force (or the curvature): regions of maximum interface elevation correlate with regions of minimum (negative) capillarity force. In this case, gravity produces a distribution of the interface elevation that in turn determines the value of the interface curvature and of F_γ. For decreasing $\sqrt{Fr}/We$ (simulation S3, Fig. 9b), the JPDF presents a broader area, typical of uncorrelated variables (F_γ changes almost independently of η). This sug-
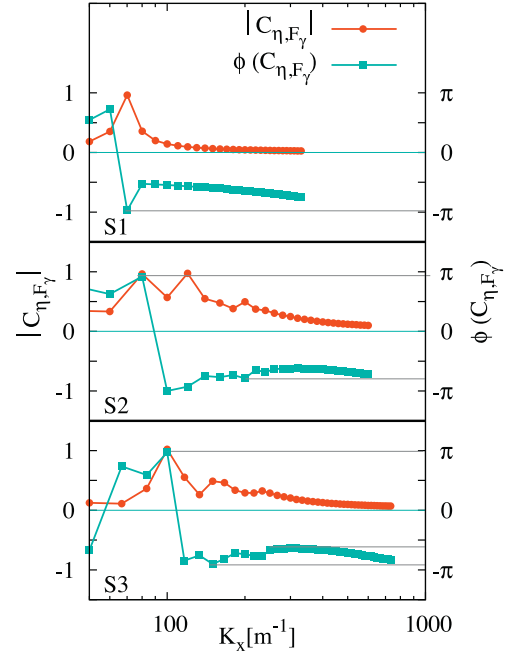
gests that for capillary-dominated waves the interface deformation behaves like a random roughness superposed on underlying longer waves.

To quantify explicitly the phase correlation between η and F_γ, we compute the coherency spectrum as

$$coh_{\eta,F_\gamma}(\tau) = \int_{-\infty}^{\infty} R_{\eta,F_\gamma}(s)\exp(-2\pi js\tau)ds. \qquad (19)$$

with R_{η,F_γ} the correlation coefficient between η and F_γ. Results are shown in Fig. 10 for all the simulations. The magnitude of the coherency spectrum ($|coh_{\eta,F_\gamma}|$, $-\bullet-$ in Fig. 10) gives an indication of the dominant wavenumbers of both signals, whereas the phase of the coherency spectrum ($\phi(coh_{\eta,F_\gamma})$, $-\blacksquare-$ in Fig. 10) measures the phase delay between the two signals. Note that the phase diagram $\phi(coh_{\eta,F_\gamma})$ is meaningful only when the magnitude of the signal $|coh_{\eta,F_\gamma}|$, develops a peak. For $\sqrt{Fr}/We = 2.16$ (S1), when $|coh_{\eta,F_\gamma}|$ is maximum (i.e for $k_x \simeq 75$), $\phi(coh_{\eta,F_\gamma}) = -\pi$, indicating a sharp phase opposition between η and F_γ. The situation changes for decreasing $\sqrt{Fr}/We$ (simulations S2 and S3). In this case, we observe peaks in the coherency spectrum occurring also at larger wavenumbers ($100 < k_x < 300\,\mathrm{m}^{-1}$). The corresponding phase delay associated to these peaks is different from $\pm\pi$ (dotted lines in Fig. 10), indicating that η and F_γ are not in opposition of phase. This situation is due to the emergence of short capillary (parasitic) waves on top of longer gravity waves: capillarity F_γ (or equivalently the curvature $\nabla \cdot n$) changes sign even though η is always positive, hence introducing a phase decorrelation between η and F_γ. The generation of ripples and the corresponding phase decorrelation between the interface elevation η and the capillarity F_γ is responsible for the shift toward larger k, which was observed in the wavenumber spectrum for $\sqrt{Fr}/We = 1.4$ (Fig. 7).

4. Conclusions and future development

We used direct numerical simulation to analyze the wave-decay process in a sheared air/water turbulent flow. Air and water were forced by an imposed pressure gradient to flow in opposite

directions (countercurrent configuration). We employed a boundary fitted technique to track the interface deformation under the combined effect of shear, pressure, surface tension and gravity. We let the air/water system evolve starting from an initial wavy interface and reducing the interfacial shear. An initial exponential decay was observed. Depending on the value of the physical parameters, chiefly $\sqrt{Fr}/We$, the spectral properties of waves changed in time during the decay process. In particular, for $\sqrt{Fr}/We < 2$ we observed that the interfacial energy contained at small wavenumbers was partially transferred towards larger wavenumbers (blue shift). This effect was only visible for small $\sqrt{Fr}/We$ (when capillary effects are important compared to gravity). At the end of the transient decay, a new asymptotic steady state condition was reached. Wavenumber spectra computed during the transient decay and at the new steady condition were found in fair agreement with the predictions given by wave turbulence theory. These results can be explained considering that the energy to sustain capillary waves is small compared to the energy contained in the most energetic waves. Therefore, although a large proportion of the energy is damped by viscous dissipation and decays exponentially in time, there is still enough energy to feed the power law cascade towards the smallest scales at any time instant. We finally considered the local interface curvature and related statistics to discuss the role of gravity and surface tension in determining the interface deformation. For $\sqrt{Fr}/We > 2$ we found that gravity was important compared to surface tension and the interface deformation was close to a sinusoidal wave propagating along the direction imposed by the mean shear. For $\sqrt{Fr}/We > 2$, capillary effects increased and the interface deformation was more isotropic (surface roughness). Present results are particularly important because they open new perspectives to analyze the dynamics of organic matter (Lovecchio et al., 2013; 2014) in realistic models of terrestrial water bodies, and to characterize the direct/inverse energy cascade process (Lovecchio et al., 2015) occurring at a deformable air/water interface.

Acknowledgments

References

Alves, J.G.M., Banner, M.L., Young, I.R., 2003. Revisiting the Pierson-Moskowitz asymptotic limits for fully developed wind waves. J. Phys. Oceanogr. 33, 1301.

Bedard, R., Lukaschuk, S., Nazarenko, S., 2013. Non-stationary regimes of surface gravity wave turbulence. JETP Lett. 97, 529.

Berhanu, M., Falcon, E., 2013. Space-time-resolved capillary wave turbulence. Phys. Rev. E 87, 033003.

De Angelis, V., Lombardi, P., Banerjee, S., 1997. Direct numerical simulation of turbulent flow over a wavy wall. Phys. Fluids 9, 2429.

Deike, L., Berhanu, M., Falcon, E., 2012. Decay of capillary wave turbulence. Phys. Rev. E 85, 066311.

Deike, L., Popinet, S., Melville, W.K., 2015. Capillary effects on wave breaking. J. Fluid Mech. 769, 541.

Dyachenko, A.I., Korotkevich, A.O., Zakharov, V.E., 2004. Weak turbulence Kolmogorov spectrum for surface gravity waves. Phys. Rev. Lett. 92, 134501.

Falcon, E., Fauve, S., Laroche, C., 2007b. Observation of intermittency in wave turbulence. Phys. Rev. Lett. 98, 154501.

Falcon, E., Laroche, C., Fauve, S., 2007a. Observation of gravity-capillary wave turbulence. Phys. Rev. Lett. 98, 094503.

Falkovich, G.E., Ya Shapiro, I., Shtilman, L., 1995. Decay turbulence of capillary waves. Europhys. Lett. 29, 1.

Fulgosi, M., Lakehal, D., Banerjee, S., De Angelis, V., 2003. Direct numerical simulation of turbulence in a sheared air-water flow with a deformable interface. J. Fluid Mech. 482, 319.

Guo, X., Shen, L., 2010. Interaction of a deformable free surface with statistically steady homogeneous turbulence. J. Fluid Mech. 658, 33.

Janssen, P.A.E.M., 2004. The Interaction of Ocean Waves and Wind. Cambridge University Press.

Kolmakov, G.V., 2006. Decay of capillary turbulence on the surface of a viscous liquid. JETP Lett. 83, 58.

Kundu, P.K., Cohen, I.M., Dowling, D.R., 2012. Fluid Mechanics, 5th ed. Academic Press, Waltham, MA.

Lombardi, P., De Angelis, V., Banerjee, S., 1996. Direct numerical simulation of near-interface turbulence in coupled gas-liquid flow. Phys. Fluids 8, 1643.

Lovecchio, S., Marchioli, C., Soldati, A., 2013. Time persistence of floating particle clusters in free-surface turbulence. Phys. Rev. E 88, 033003.

Lovecchio, S., Zonta, F., Soldati, A., 2014. Influence of thermal stratification on the surfacing and clustering of floaters in free surface turbulence. Adv. Water Resour. 72, 22.

Lovecchio, S., Zonta, F., Soldati, A., 2015. Upscale energy transfer and flow topology in free surface turbulence. Phys. Rev. E 91, 033010.

Miquel, B., Mordant, N., 2011. Nonstationary wave turbulence in an elastic plate. Phys. Rev. Lett. 107, 034501.

Pushkarev, A.N., Zakharov, V.E., 1996. Turbulence of capillary waves. Phys. Rev. Lett. 76, 3320.

Soldati, A., Banerjee, S., 1998. Turbulence modification by large-scale organized electrohydrodynamic flows. Phys. Fluids 10, 1743.

Zakharov, V.E., L'vov, V., Falkovich, G., 1992. Kolmogorov Spectra of Turbulence I.. Springer-Verlag, Berlin.

Zonta, F., Onorato, M., Soldati, A., 2012. Turbulence and internal waves in stably-stratified channel flow with temperature-dependent fluid properties. J. Fluid Mech. 697, 175.

Zonta, F., Soldati, A., Onorato, M., 2015. Growth and spectra of gravity-capillary waves in countercurrent air-water turbulent flow. J. Fluid Mech. 777, 245.